Check for updates

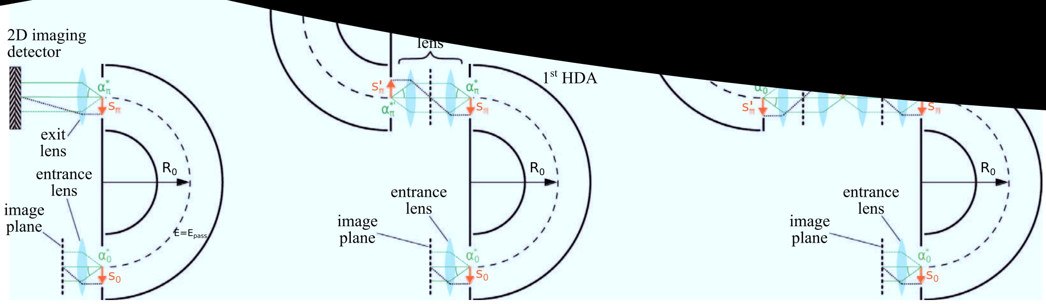

Fig. 1. Electron optical layout of different configurations of the hemispherical deflection analyzer (HDA) for imaging applications. a) Single HDA. b) Aberration compensated double HDA arrangement with an inverting transfer lens. c) Double pass HDA with a non-inverting transfer lens. Thick dotted lines mark the image planes as projected on the 2D imaging detector. Arrows (s_n) denote the electron distributions in the entrance and exit slit planes.

images, the spatial intermediate image of the sample surface is located in the plane indicated by the dotted line in Fig. 1a, and an image of the transverse momentum distribution of the photoelectrons is projected onto the entrance slit of the analyzer.

The two-dimensional spatial coordinates (x, y) are therefore encoded in the entrance angles (β_0, α_0) of the electrons passing through the slit. As outlined in Ref. [3] this relation is reversed when recording momentum images. The momentum microscope projects a real space image onto the entrance slit of the electron analyzer, such that the two-dimensional momentum distribution of the photoelectrons (k_x, k_y) is encoded in the two orthogonal entrance angles (β_0, α_0). In general, the intermediate image in the entrance plane of the analyzer is always reciprocal to the image that shall be recorded on the detector of the microscope. In that way, the small entrance stilt does not restrict the field of view of the measured image.

Under the assumption that the entrance angles of the electron trajectories are preserved upon passing through the analyzer, the exit lens can recover the 2D image information after the energy selection, and project the image plane onto the detector. As was pointed out, however, for instance in Ref. [7], the angle α_0 is not strictly conserved, but is subject to the α^2 aberration term inherent to the HDA. This effect would limit the obtainable image resolution.

Fig. 1b shows the scheme of an imaging double hemispherical analyzer. The energy selection is, as in (a), entirely performed by the first HDA. The compensation of the α^2 aberration of the analyzer is then accomplished by an inverted beam path in the second HDA [8,9]. Electrons that leave the 1st HDA through the exit slit are projected into the entrance slit of the 2nd HDA by an inverting transfer lens with magnification $M = -1$. In this scheme, electron trajectories correspond to closed Kepler orbits, such that perfect refocusing of electron trajectories at the exit of the double HDA is obtained. In the exit plane of the 2nd HDA therefore also the energy dispersion vanishes. Refocusing is not limited to the spatial coordinates, but also with respect to the time-of-flight of the electrons inside the analyzer, such that the ToF does not depend on the entrance angle, i. e., the position in the 2D image [10]. Together with straight drift sections therefore a completely isochronous analyzer can be realized [11].

Fig. 1c shows a second type of a double HDA arrangement, which does not employ the aforementioned aberration compensation. In contrast to Fig. 1b, the transfer lens located between the two hemispheres is non-inverting, i. e., with a magnification of $M = 1$, in the case of two identical hemispheres [12]. Compared to the aberration compensated analyzer, this setup results in a double pass arrangement, where the dispersion of both analyzers adds up, resulting in an improved energy resolution [13]. The energy of the transmitted electrons is then defined by the entrance slit of the 1st HDA and the exit slit of the 2nd HDA. Using a suitable transfer lens between the hemispheres further allows to switch between the aberration compensated configuration in Fig. 1b and the double pass configuration in 1c.

Here, we discuss the imaging properties of the hemispherical deflection analyzer based on analytical solutions of the electron trajectories. Including the effect of the fringe fields at the entrance and exit of the analyzer, we show that refraction leads to a full conservation of the trajectory angle α. This previously overlooked effect eliminates the α^2 aberration from the energy filtered images and allows for more compact imaging energy filters for momentum microscopy or photoelectron emission microscopy. We present first experimental results of the new double pass configuration of the double HDA for the momentum microscope, resulting in unsurpassed energy resolution and measurement efficiency.

2. Electrons in the hemispherical analyzer

First of all, we describe the electron trajectories inside the hemispherical electron analyzer in an analytical model. Fig. 2a shows the definition of coordinates inside the analyzer. Due to the spherical symmetry, a spherical coordinate system is used, with $r(\varphi)$ being the radius from the center as a function of the deflection angle φ. The start radius at $\varphi = 0$ and the radius after $\varphi = 180^\circ$ deflection is r_0 and r_π, respectively. The starting angle within the plane of motion is α_0 (see Fig. 2b), and β_0 perpendicular to this plane (see Fig. 2c). Without loss of generality, the motion of electrons always takes place within the plane shown in Fig. 2a, such that the complete electron trajectory is given by $r(\varphi)$.

The electron motion inside the analyzer is governed by the $\sim \frac{1}{r}$ potential of the spherical electrodes:

$$U(r) = U_0 \frac{R_0}{r}, \tag{1}$$

where R_0 is the nominal mean radius and $U_0 < 0$ the electrostatic potential at the mean radius. The electrostatic potential of the inner and outer electrodes then is given by

$$U_i = U_0 \frac{R_0}{R_i}, \quad U_a = U_0 \frac{R_0}{R_a}. \tag{2}$$

The solution of the equation of motion of a particle in a $\sim \frac{1}{r}$ potential is a well know problem of classical mechanics. In general, the trajectories are given by conic sections, whereas the bound solutions, i. e., with finite r, are Kepler ellipses. Therefore, we will here only briefly recall the solution of the equation of motion as far as it is relevant for analyzing the imaging properties of the electron spectrometer. For a detailed description of the Kepler problem, we refer to

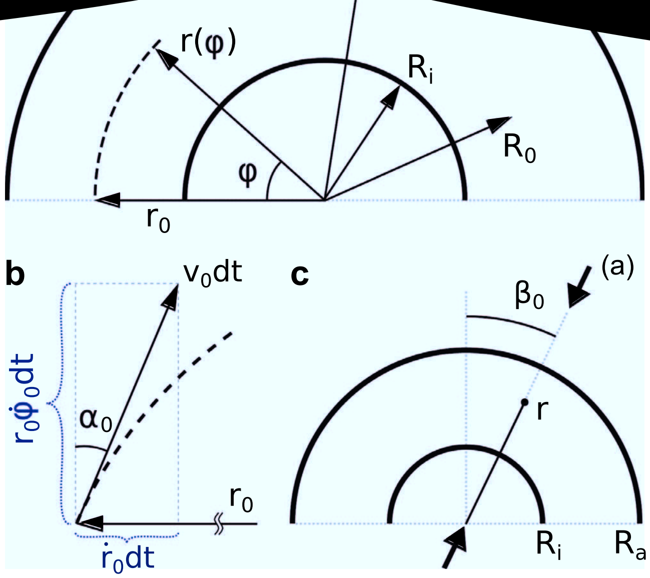

Fig. 2. a) Spherical coordinate system of the hemispherical analyzer. Capital letters denote the nominal center radius, R_0, and the radii of the inner and outer hemispherical electrode, R_i and R_a, respectively. The electron trajectory with radius $r = r(\varphi)$ is described in spherical coordinates with the start radius r_0, the angle φ, and the exit radius r_π. b) Starting angle α_0 expressed by the radial ($\dot{r}$) and angular ($\dot{\varphi}$) velocity. c) The starting angle β_0 defines the plane of motion in the spherical symmetric potential.

classical mechanics textbooks.

The formulation of the equation of motion becomes particularly straightforward by identifying the fundamental conservation laws of the system. First of all, this is the conservation of the total energy, E_{tot}:

$$E_{tot} = U + T = const. \quad \Leftrightarrow \quad \dot{E}_{tot} = 0\,, \tag{3}$$

with the potential energy U and the kinetic energy T. As outlined in Fig. 2b, the velocity of the electrons can be written as $v = \sqrt{\dot{r}^2 + r^2\dot{\varphi}^2}$ using radial coordinates. Then the kinetic energy becomes

$$T = \frac{1}{2}m_e v^2 = \frac{1}{2}m_e(\dot{r}^2 + r^2\dot{\varphi}^2), \tag{4}$$

with the electron mass m_e.

Due to the spherical symmetry of the analyzer, also the total angular momentum is conserved.

$$L = m_e r^2\dot{\varphi} = const. \quad \Leftrightarrow \quad \dot{L} = 0 \tag{5}$$

$$L^2 = m_e^2 r^4\dot{\varphi}^2 = 2m_e r^2\left(T - \frac{m_e}{2}\dot{r}^2\right) \tag{6}$$

Comparing Eqs. (4) and (5), one can then write the kinetic energy as

$$T = \frac{L^2}{2m_e r^2} + \frac{m_e}{2}\dot{r}^2. \tag{7}$$

By inserting Eqs. (1) and (7) into Eq. (3) we obtain the equation of motion of the electrons in the hemispherical analyzer:

$$E_{tot} = U_{eff} + \frac{m_e}{2}\dot{r}^2 \qquad \text{and} \qquad \dot{E}_{tot} = 0, \tag{8}$$

with the effective potential

$$U_{eff} = U_0\frac{R_0}{r} + \frac{L^2}{2m_e r^2}. \tag{9}$$

$$\frac{dU_{eff}}{dr}|_{r=r_0} = 0 \quad \Leftrightarrow \quad -U_0\frac{R_0}{r_o^2} - \frac{}{m_e r_0^3} = 0. \tag{10}$$

Using Eq. (7), we can replace the angular momentum L by the constant kinetic energy T_0 of the circular orbit, and obtain the result

$$U_0 = -2\frac{r_0}{R_0}T_0 \tag{11}$$

Electrons that fly through the hemispherical analyzer on a circular trajectory with a radius equal to R_0 are nominally allowed to pass through the exit slit of the analyzer, and being recorded on the detector. This condition therefore defines the pass energy, E_{Pass}, of the electrons for normal incidence ($\alpha_0 = 0$). Therefore, choosing $r_0 = R_0$ and the kinetic energy $T_0 = E_{Pass}$, we obtain the pass energy of the analyzer for a given value of the electrode potentials:

$$E_{Pass} = -\frac{U_0}{2} \tag{12}$$

The respective potentials of the inner and outer hemispherical electrode, required to set this pass energy, are then given by Eq. (2).

2.2. General solution of the equation of motion

For the general description of the imaging properties of the hemispherical analyzer, we need to find the solution $r(\varphi)$ of Eq. (8) for the start parameters α_0, r_0, and T_0 at the entrance of the analyzer at $\varphi = 0$. As shown in Fig. 2b, this also defines the start velocities $\dot{\varphi}_0$ and $\dot{r}_0$ by

$$\dot{\varphi}_0 = \cos\alpha_0\cdot\sqrt{\frac{2T_0}{m_e}}\frac{1}{r_0} \quad \text{and} \quad \dot{r}_0 = \sin\alpha_0\cdot\sqrt{\frac{2T_0}{m_e}}\,, \tag{13}$$

and the angular momentum

$$L^2 = 2m_e r_0^2 T_0\cos^2\alpha_0. \tag{14}$$

A detailed solution of the equation of motion of a particle in the $\frac{1}{r}$ potential is, for instance, given in Ref. [14]. In the Lagrange formalism of classical mechanics, the solution can be obtained by solving the differential equation

$$\frac{d\varphi}{dr} = \frac{d\varphi}{dt}\frac{dt}{dr} = \frac{L}{m_e r^2}\frac{dt}{dr}. \tag{15}$$

The derivative $\dot{r} = \frac{dr}{dt}$ that appears in this expression is obtained from Eq. (8):

$$\frac{dr}{dt} = \sqrt{\frac{2}{m_e}(E_{tot} - U_0\frac{R_0}{r} - \frac{L^2}{2m_e r^2})}\,. \tag{16}$$

The solution of the electron trajectory then can be directly obtained by integration of Eq. (15):

$$\varphi = \int dr\frac{L}{r^2\sqrt{2m_e E_{tot} - 2m_e U_0\frac{R_0}{r} - \frac{L^2}{r^2}}} \tag{17}$$

Eq. (17) can be solved using common tabulated integrals. For instance, the solution of Eq. (17) can be also easily obtained by using the substitution $u = \frac{1}{r}$, and integration over $\int du$ [15]. The result then defines the electron trajectory $r(\varphi)$ as a function of the deflection angle φ inside the analyzer, where φ′ is the constant integration parameter:

$$1 + \cos(\varphi + \varphi')\sqrt{\frac{2E_{tot}L^2}{m_e U_0^2 R_0^2} + 1} = -\frac{L^2}{m_e U_0 R_0}\frac{1}{r} \tag{18}$$

This expression still contains the constants for the total energy and

[redacted]

$$r_0 T_0 \quad + 1)\cdot 4r_0 T_0$$

$$= -2r_0^2 T_0 \cos^2\alpha_0 \frac{1}{r} \tag{19}$$

For the following discussion, it is useful to introduce the dimensionless variables ρ and η for the radius and kinetic energy, respectively:

$$\rho = \frac{r}{R_0} \quad \text{and} \quad \eta = \frac{T}{E_{pass}} = -\frac{2T}{U_0}, \ \text{with}\, \eta, \rho \geq 0 \tag{20}$$

With this definitions, Eq. (19) can be simplified to

$$\frac{\rho}{\rho_0} = \frac{\kappa}{1 + \varepsilon\cos(\varphi + \varphi')}, \tag{21}$$

where we use the additional abbreviations

$$\begin{aligned} \kappa &= \rho_0\eta_0\cos^2\alpha_0 \qquad \text{and} \\ \varepsilon &= \sqrt{(1-\rho_0\eta_0)^2 + (2\rho_0\eta_0 - \rho_0^2\eta_0^2)\sin^2\alpha_0}\,. \end{aligned} \tag{22}$$

Since the electron trajectory starts at $\varphi = 0$ with the radius $\rho_0 = r_0/R_0$, we can now determine the integration parameter as $\varepsilon\cos(\varphi') = \kappa - 1$, thus describing the complete electron trajectory inside the analyzer. For discussing the imaging parameters of the analyzer, in the following, we look at the solution at the exit of the analyzer, i. e., after a deflection angle of 180°. Then, the radius ρ_π at the exit of the analyzer, and the radius change Δρ are given by

$$\frac{\rho_\pi}{\rho_0} = \frac{\kappa}{1 - \varepsilon\cos(\varphi')} = \frac{2}{2-\kappa} - 1 \tag{23}$$

and

$$\frac{\Delta\rho}{\rho_0} = \frac{2}{2-\kappa} - 2\,. \tag{24}$$

As we can see from this result, the position at which the electron arrives at the exit of the analyzer depends first of all on the kinetic energy η_0, and also on the starting angle α_0. In particular the angular dependence is given by $\cos^2\alpha_0$, such that electrons with a non-zero start angle always arrive at a smaller radius compared to electrons with the same energy, but normal incidence ($\alpha_0 = 0$). This result is known as the α^2 aberration of the electrostatic HDA, and as we will see below, has important implications on the energy resolution of the analyzer.

The result further shows that the image obtained after a deflection angle of 180° in the exit plane of the analyzer is dispersed in energy along the radial direction. Due to the spherical symmetry, however, no dispersion occurs in the second in-plane direction, normal to the $r - \varphi$ plane. Therefore, placing a two-dimensional detector in the exit plane of the analyzer – or projecting a direct image of this plane onto the detector – is not suitable to record a two-dimensional (x, y) electron microscope image. Instead the detector image will show one spatial coordinate along the non-dispersive direction, and the electron energy spectrum along the radial, dispersive direction.

Therefore, as stated above, the two-dimensional image information in a (momentum) electron microscope is encoded as the entrance angle of electrons into the analyzer such that $(x,\ y) \longrightarrow (\beta_0,\ \alpha_0)$. For the image aberration that applies in that case, we have to consider how the trajectory angle α_π in the exit plane of the analyzer is related to the starting parameters ρ_0, η_0, and α_0. Since $\tan\alpha = \frac{1}{\rho}\frac{d\rho}{d\varphi}$, the trajectory angle α is obtained by calculating the derivative of Eq. (21) with respect to the deflection angle φ:

$$\frac{d\rho}{d\varphi} = -\rho\frac{\varepsilon\sin(\varphi + \varphi')}{1 + \varepsilon\cos(\varphi + \varphi')} \tag{25}$$

For $\varphi = \pi$, we therefore obtain

$$\rho_0$$

The angle α_π at the exit of the hemisphere therefore depends not only on the entrance angle α_0, but also on the position ρ_π. The latter contains a non-trivial dependence on the starting radius ρ_0, the starting angle α_0, and the kinetic energy η_0. At the first glance, this results therefore suggests an image aberration that arises due the α^2 aberration, even when the image information is transferred through the angular coordinate. This result up to here is the same as was derived earlier in Ref. [7], and termed *sphere aberration*, limiting the image resolution in microscopy applications of the hemispherical deflection analyzer.

3. Hemispherical analyzer with slits

So far, we have described the movement of an electron inside the radial potential of the hemispherical analyzer. This description shows important properties of the electron analyzer, such as the energy dispersion, and the aberration with respect to the entrance angle α_0. In order to consider the image aberrations in the case of the application in an electron microscope, however, an important aspect has so far been neglected. This is the transition of the electrostatic potential when the electrons enter the analyzer at the entrance slit, and when the electrons leave the analyzer at the exit slit. In general, we assume for the following considerations that the entrance- and exit-slits of the analyzer have a finite width in the radial direction.

At the entrance slit, as well as at the exit slit, electrons pass from a constant potential $U^* = U_0$ over to the spherically symmetric potential $U(r) \sim \frac{1}{r}$. Depending on the radius r, electrons therefore are accelerated or decelerated upon entering the analyzer. Fig. 3 illustrates this refraction at the slits, which happens both, at the entrance and exit of the analyzer. The entrance angle α_0^* outside of the analyzer therefore changes due to the refraction towards larger or smaller values α_0 for $r > R_0$ or $r < R_0$, respectively. Here and in the following, starred variables always refer to values outside, and their non-starred counterpart to the respective value inside of the analyzer.

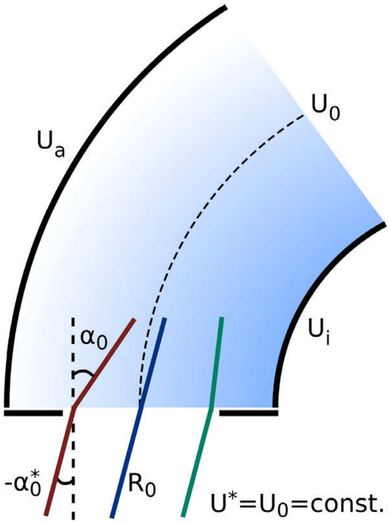

Fig. 3. Refraction of electron trajectories at the transition from a constant electrostatic potential $U^* = U_0$ outside of the analyzer to a spherical symmetric potential $U \sim \frac{1}{r}$ inside of the analyzer. Depending on the radius, the angle α_0 inside the analyzer becomes larger or smaller compared to the angle α_0^* outside the analyzer.

$$\frac{}{E_{pass}\,\rho_n} + \frac{U_0}{E_{pass}} = \eta_n^* + \frac{2}{\rho_n} - 2,$$

where $n = 0,\ \pi$ at the entrance and exit of the analyzer, respectively. Outside of the analyzer the kinetic energies of the electrons are equal due to energy conservation, such that $\eta_0^* = \eta_\pi^* \equiv \eta$.

When the potential transition at the slit takes place only in the direction normal to the slit plane, the transverse momentum of electrons is conserved, such that $\dot{r}$=$\dot{r}$*. Then, from Eq. (13) follows that the trajectory angle changes as

$$\sin^2\alpha_n = \sin^2\alpha_n^* \frac{\eta}{\eta_n}. \tag{29}$$

With this result, we can now reformulate the expression for the analyzer dispersion that we have derived in Eq. (24) using the angle α_0^* outside of the analyzer. This results in the more useful expression

$$\frac{\Delta\rho}{\rho_0} = \frac{2}{\rho_0(2 - \eta + \eta\sin^2\alpha_0^*)} - 2, \tag{30}$$

using the true entrance angle α_0^* into the analyzer.

In the next step, we derive the exit angle α_π^* after the electron has passed the exit slit. First of all, the expression for the angular momentum in Eq. (14) applies both, at the entrance and at the exit of the analyzer. Due to the conservation of angular momentum, it therefore follows that $\rho_0\sqrt{\eta_0}\cos\alpha_0 = \rho_\pi\sqrt{\eta_\pi}\cos\alpha_\pi$. When we insert this relation into the expression for the sphere aberration of the angles in Eq. (27) we get

$$\sin\alpha_\pi = -\sqrt{\frac{\eta_0}{\eta_\pi}}\sin\alpha_0, \tag{31}$$

which has a similar form as Eq. (27). However, inserting now Eq. (29) for the refraction at the slit for $\sin\alpha_0$ and $\sin\alpha_\pi$, we get

$$\sin\alpha_\pi^* = -\sin\alpha_0^*. \tag{32}$$

This result reveals that the refraction of electrons at the potential transition at the slits leads exactly to the cancellation of the sphere aberration term for the trajectory angle α. Without the refraction effect, the sphere aberration in Eq. (27) would only vanish in the hypothetical limiting case of zero-width slits, i.e., for $\rho_\pi = \rho_0$. However, Eq. (32) shows that even for a finite slit width the fringe field, introduced by the transition of the electrostatic potential at the entrance- and exit-slits, leads to a conservation of the trajectory angle $\alpha_0^* = -\alpha_\pi^*$. Therefore, our result shows that the hemispherical analyzer does not introduce an image aberration, as long as the image information is encoded as the entrance angle, or alternatively as the transverse momentum (i. e., $\dot{r}$*) of the incoming electron ensemble.

The fringe fields that arise due to the transition between the spherical $U(r) \sim \frac{1}{r}$ potential inside the analyzer to the constant potential U^* outside the analyzer are known to lead to a focusing of the trajectories in the entrance and exit regions [16]. This focusing effect shifts the focal point to deflections angles φ < 180°, such that the crossover of the trajectories lies inside the analyzer in front of the slit plane [17,18]. This focusing effect is directly related to the refraction of the trajectories described here. In Fig. 3, this leads to a crossover of a parallel set of trajectories inside the HDA. The canceling of image aberrations thus is a direct consequence of the presence of the fringe field, as long as the entrance angle α_0^* stays sufficiently small such that higher order aberrations by the fringe fields can be neglected. As we will shown below, this applies well for entrance angles up to several degrees.

We note that the same result can be also obtained without the detailed calculation of the refraction angles, but by considering the fundamental conservation laws of the system. Due to energy conservation, we obtained outside of the analyzer $\eta_0^* = \eta_\pi^* \equiv \eta$. In addition, as

mentum

4. Energy resolution

The energy resolution of the analyzer is determined by the width of the entrance-slit located at $\varphi = 0$ and exit-slit located at $\varphi = 180°$. The width of the slits are d_1 and d_2, respectively. In dimensionless variables, the slit width then is given by

$$\delta_1 = \frac{d_1}{R_0} \quad \text{and} \quad \delta_2 = \frac{d_2}{R_0}. \tag{33}$$

When both slits are located symmetric with respect to the nominal radius R_0 the possible range of entrance and exit radii, i. e., of those electrons that are allowed to pass through the slit, is then given by

$$\rho_0 = [1 - \frac{\delta_1}{2}, 1 + \frac{\delta_1}{2}], \quad \text{and} \quad \rho_\pi = [1 - \frac{\delta_2}{2}, 1 + \frac{\delta_2}{2}]. \tag{34}$$

For simplicity, we assume that the slits have sharp edges. This is the case when the roughness of the slit edge, and the thickness of the slit is much smaller than the width d of the slit. In that case, the cutoff of electrons at the slit edge becomes a step function as displayed in Fig. 4a.

Only those electrons are transmitted through the analyzer that have a radial coordinate within the interval of the allowed start radius ρ_0, and after a deflection angle of 180° arrive at a ρ_π lying within the interval of the allowed exit radius. Fig. 4b shows the resulting transmission function in this model of ideal sharp slits. The transmission can be described as a function of the radial dispersion $\Delta\rho$, as defined above in Eq. (30), $Tr = Tr(\Delta\rho)$. From Fig. 4b we estimate the full width at half maximum (FWHM) of $Tr(\Delta\rho)$ as $\Delta\rho_{FWHM} \approx \frac{\delta_1+\delta_2}{2} + |\frac{\delta_1-\delta_2}{2}|$. The best effective transmission for a given FWHM is obtained for equally wide slits, $\delta_1 \approx \delta_2$. In this case, we can approximate the FWHM as

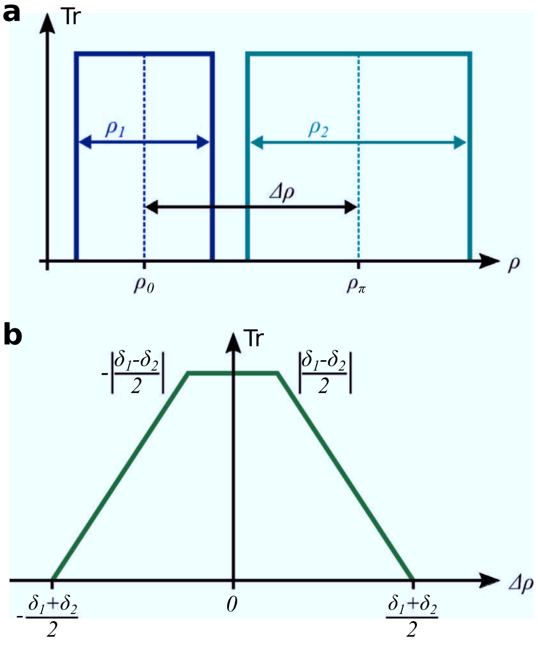

Fig. 4. a) Ideal transmission, *Tr*, through the entrance and exit slits, as a function of the radial coordinate. b) Effective transmission function of the analyzer as function of the change of the radial coordinate Δρ upon 180° deflection.

erivative of Eq. (30):

$$d\eta = \frac{\partial \eta}{\partial \rho_\pi} d\rho + \frac{\partial \eta}{\partial \sin^2 \alpha_0^*} d \sin^2 \alpha_0^* \; , \tag{36}$$

where the partial derivatives $\frac{\partial \eta}{\partial \rho_\pi}$ and $\frac{\partial \eta}{\partial \sin^2 \alpha_0^*}$ are both evaluated with $\rho_\pi = \rho_0 = 1$ and $\sin^2 \alpha_0^* = 0$.

Inserting Eq. (30), this evaluates to $d\eta = \frac{1}{2} d\rho + d \sin^2 \alpha$, where $d\rho = \Delta\rho_{FWHM} \approx \frac{\delta_1 + \delta_2}{2}$ and for small entrance angles we use the approximation $d \sin^2 \alpha_0^* \approx (\alpha_{0,max}^*)^2$. Here, $\alpha_{0,max}^*$ is the maximum value of the entrance angle, which lies in the interval $\alpha_0^* = [-\alpha_{0,max}^*, \; \alpha_{0,max}^*]$. The energy resolution of the analyzer then is given by

$$\frac{\Delta E}{E_{Pass}} = \frac{1}{2} \frac{\delta_1 + \delta_2}{2} + {\alpha_{0,max}^*}^2 . \tag{37}$$

4.1. *Energy resolution of the imaging HDA*

The energy resolution given in Eq. (37) applies for conventional analyzers that integrate over the complete angular interval $\alpha_0^* = [-\alpha_{0,max}^*, \; \alpha_{0,max}^*]$. This is the case for conventional, non-imaging electron spectrometers. For such spectrometers the exit slit is eventually replaced by a 2D electron detector to record simultaneously the energy spectrum that is projected in the exit plane [5]. In the case of such angle integrating spectrometers, the distribution of entrance angles $\pm\, \alpha_{0,max}^*$ limits the ultimate energy resolution. An improvement of the energy resolution then requires not only to reduce the width of the entrance and exit slits, but also to restrict the accepted angular interval $\pm\, \alpha_{0,max}^*$ at the expense of the transmission of the spectrometer.

This expression, however, does not apply to imaging energy analyzers. As we have already seen above, the imaging electron analyzer maps the angular coordinate $\pm\, \alpha_0^*$ to the spatial coordinate $\pm\, y$ on the image detector that follows behind the exit slit. When we assume that one resolves about 400 image points across the diagonal of the detector, the angular interval for each point becomes $d\alpha_0^* \approx \frac{\alpha_{0,max}^*}{200}$. This value becomes negligible small for typical angular intervals of the transferred image in the order of $\alpha_{0,max}^* \approx 3^\circ$. In Eq. (36) we therefore insert $d \sin^2 \alpha_0^* = 0$, and the energy resolution of the imaging analyzer becomes for each point in the image

$$\frac{\Delta E}{E_{Pass}} = \frac{1}{2} \frac{\delta_1 + \delta_2}{2} . \tag{38}$$

Nevertheless, since each point in the image along the y coordinate corresponds to a different α_0^* the 2D image recorded on the detector does not strictly correspond to a constant kinetic energy of the electrons. The angular dependence of the kinetic energy with ($\Delta\rho = 0$ and $\rho_0 = 1$) that can pass the analyzer is given by Eq. (30):

$$\eta_{Pass}^{\alpha}(\alpha_0^*) = \frac{1}{1 - \sin^2 \alpha_0^*} \approx 1 + (\alpha_0^*)^2 \tag{39}$$

The contribution of terms of $\mathcal{O}(\alpha_0^*)^4$ is less than 0.1% for entrance angles $\leq 10^\circ$, and thus can be neglected. The value $\eta_{Pass}^{\alpha} = \frac{E_{Pass}(\alpha_0^*)}{E_{Pass}(\alpha_0^* = 0)}$ can be interpreted as the effective pass energy that varies over the image field as the entrance angle α_0^* varies.

Fig. 5 shows the variation of the effective pass energy as function of α_0^*. For $\alpha_0^* = 0$ the energy of the transmitted electrons equals the nominal pass energy as defined above. For all other entrance angles, electrons need an energy larger than the nominal pass energy in order to pass through the analyzer. The figure shows that this variation of the effective pass energy is in the order of up to 0.3% for the range of entrance angles between − 3° and + 3°. At the same time, error bars indicate the energy resolution at each image point as derived from Eq. (38) with a slit width of $\delta_{1,2} = 0.2\%$ of the mean radius, i. e., a slit width of 0.2 mm for an analyzer with $R_0 = 100$ mm. For such parameters, the energy resolution is considerably better than the variation of the pass energy, and the non-constant pass energy needs to be considered. If the slit width is increased to values of the order of 1% of the analyzer radius, the $(\alpha_0^*)^2$ term becomes negligible compared to the energy resolution defined by the slits. In the case of the momentum microscope, the size of the entrance slit, δ_1, demagnified by the microscope imaging column, also defines the analyzed area on the sample surface [3].

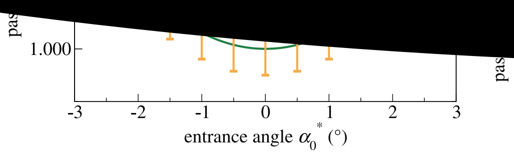

Fig. 5. Nonisochromaticity as a function of the entrance angle α_0^* (solid line). The bars indicate the energy resolution at each image point as in Eq. (38). The left scale displays the effective pass energy $\eta_{Pass}^{\alpha}(\alpha_0^*)$, whereas the nominal pass energy corresponds to $\eta = 1$. The right scale shows the energy shift relative to a pass energy of $E_{Pass} = 50$ eV.

The effect of the pass energy being not constant over the image is often also termed *nonisochromaticity*, generally describing the energy variation over the field of view of an imaging energy analyzer. In the context of high resolution transmission electron microscopy (TEM), the nonisochromaticity represents a well known image aberration of the electron energy filter. However, the effect usually affects all types of imaging electron energy analyzers. In the past, much effort has been taken to optimize energy filters for TEM application also with respect to the nonisochromaticity [20]. For instance, a filter with a particularly low variation of the energy over the image is the MANDOLINE filter [21] with a negligible nonisochromaticity of only 10 meV.

The origin of the nonisochromaticity are non-vanishing aberration terms in the energy dispersive plane of the analyzer. For the hemispherical analyzer this comes about the α_0 dependent terms in Eq. (21). The same effect that leads to the nonisochromaticity of the imaging analyzer, likewise leads to a degradation of the energy resolution for non-imaging spectrometers for finite acceptance angles. In this context it has been previously proposed that refocusing of trajectories with different α_0 can be achieved by biasing the electrode potentials [22] or by displacing the entrance slit [22,23]. The angle dependent term in Eq. (37) then might be compensated by the asymmetric fringe fields. For imaging analyzers, such an approach is, however, complicated by the broken symmetry and asymmetric fringe fields, that can introduce higher order aberration terms.

Fig. 6a shows the effect of the nonisochromaticity on the intensity distribution in the measured Fermi surface contour of a W(110) single crystal. The experiment was performed using s-polarized photons with a photon energy of $h\nu = 50$ eV incident along the k_y axis. The image was recorded with a fixed setting of the kinetic energy at a pass energy of the analyzer of 50 eV, and a slit width of 200 μm. This closely resembles the relative magnitude of the energy resolution and the nonisochromaticity across the image as in the discussion above. In the experiment, the energy resolution is of the order of 60 meV for the width of the Fermi edge measured at a temperature of 130 K.

Due to the variation of the effective pass energy along the y-axis, the as-measured Fermi surface contour fades out towards the top and bottom of the momentum disk. While the center at $k_y = 0$ has an energy set to the nominal Fermi level, E_F, the effective electron kinetic energy

[redacted]

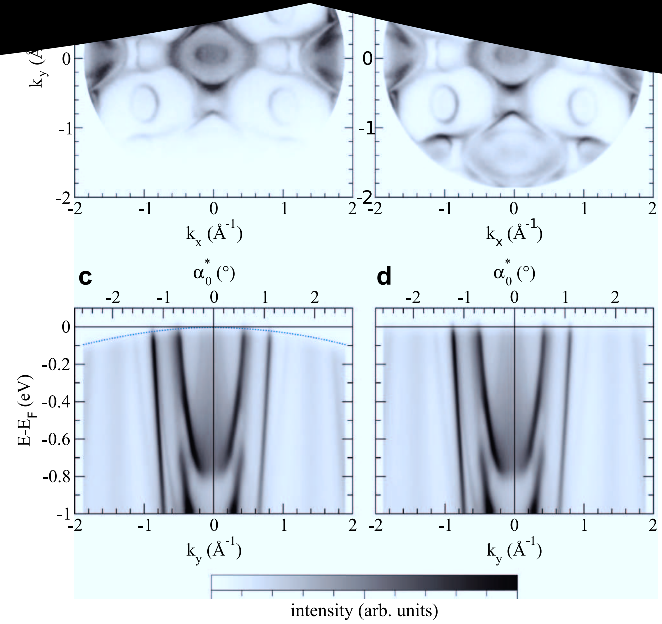

Fig. 6. Fermi surface contour of W(110) measured with s-polarized light with a photon energy of $h\nu = 50$ eV, and at a pass energy of the double hemispherical energy filter of the 50 eV. a, c) As measured Fermi surface contour and spectral function along the k_y axis. The dotted line in (c) indicates the Fermi edge as a guide to the eye. b, d) The same after applying the correction for the parabolic energy shift η^{α}_{Pass} as function of k_y to the as measured data. Intensities are displayed on a linear gray scale. The data has been measured at the NanoEsca beamline [19] at the Elettra synchrotron, Trieste, Italy.

towards larger and smaller k_y is larger than E_F. This effect is best seen in the band dispersion along the k_y axis in Fig. 6c, where the Fermi edge is parabolically bent downwards. The maximum shift of the Fermi edge in this measurement is -100 meV, slightly smaller than the value of -137 meV that is expected for $\alpha^*_{0,max} = \pm 3°$. This is due to the smaller range of entrance angles in the experiment, where the measured reciprocal space field of view of ± 1.9 Å^{-1} corresponds to $\alpha^*_{0,max} = \pm 2.6°$.

contour

rected band dispersion in Fig. 6d

straight line of the intensity cut-off.

5. The double pass imaging energy filter

Taking into account the effect of the entrance and exit slits of the HDA, we have shown that the entrance angle α^*_0, outside of the analyzer, is directly transferred from the entrance to the exit of the hemisphere. The α term in the image aberration therefore vanishes already for a single HDA. In addition, this finding enables the use of a double HDA arrangement in a double pass configuration, as shown in Fig. 1c. Due to the geometrical similarity of the double HDA setup in the case of an aberration compensated setup, or in the case of the non-aberration corrected double pass setup, we compare the performance of these two imaging energy filters.

Experiments have been carried out using the momentum microscope setup described in Ref. [3]. In the first case, the transfer lens between both hemispheres is of the inverting type, with a magnification of $M = -1$. This setup therefore uses the aberration compensated configuration of the double HDA setup, shown in Fig. 1b, such that only the first HDA equipped with 0.2 mm wide entrance and exit slits contributes to the energy resolution.

Fig. 7a shows the Fermi surface contour of a Au(111) single crystal surface, measured by illumination with He-I radiation ($h\nu = 21.22$ eV) from a focused helium discharge lamp (SPECS UVS-300). The measurement was taken with the analyzer set to a pass energy of 50 eV. The nominal energy resolution given by Eq. (38) is $\Delta E = 33$ meV, in good agreement with the experiment [3]. Under this condition, the momentum disk shown in Fig. 7a was integrated over a total measurement time of 25 minutes [3].

In the second experiment, the transfer lens of the double HDA was modified, such that a non-inverted image is projected into the entrance of the 2nd HDA. As shown in Fig. 1c, the transfer lens then consists of two telescopic sections instead of one in the case of the inverting lens. In addition, the 0.2 mm wide energy selection slit needs to be moved from the original location at the exit of the 1st HDA to the exit of the 2nd

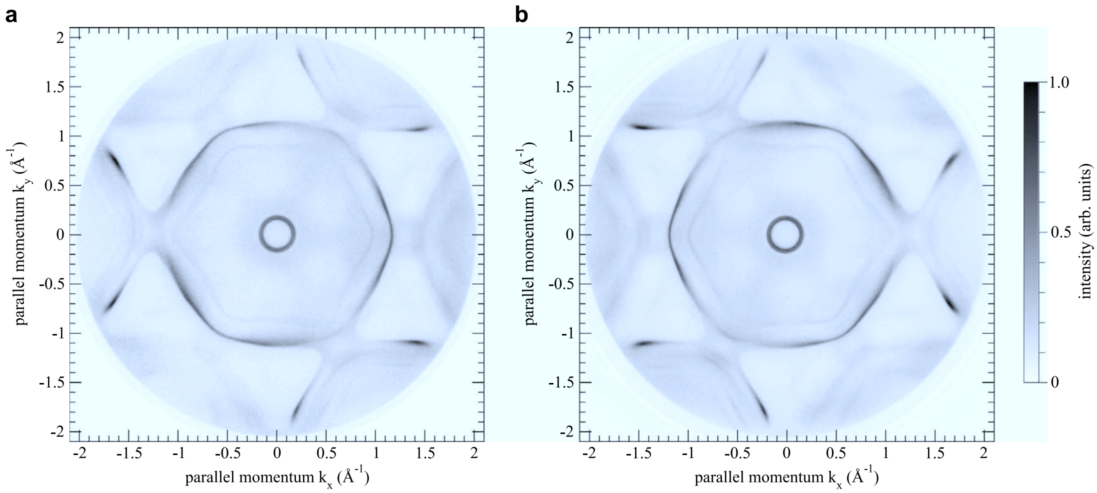

Fig. 7. Fermi surface contour of the Au(111) surface measured in the momentum microscope using illumination with He-I ($h\nu = 21.22$ eV) radiation. a) Measurement with energy analyzer set to the aberration compensated scheme at a pass energy of 50 eV and integration time of 25 min. Data as in [3]. b) The same measurement, but with the analyzer set to double pass operation and a pass energy of 30 eV and integration time of 10 min. Image rotation by 180° is due to the non-inverting transfer lens compared to (a). Intensities are displayed on a linear gray scale.

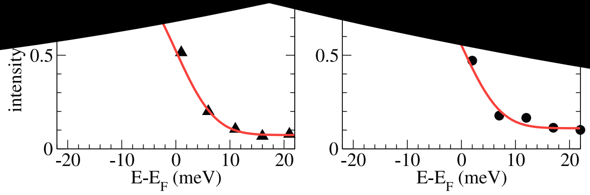

Fig. 8. a) Measured Fermi edge (symbols) at a sample temperature of 20 K using the aberration compensated configuration of the double HDA energy filter at a pass energy of 15 eV. The solid line shows a fit with a FWHM of $\Delta E = 12$ meV. b) The same, but using the double pass configuration at a pass energy of 30 eV. The fit results in $\Delta E = 13$ meV.

HDA, while the free aperture between both HDAs needs to be large enough to not block the electrons passing from one HDA to the other.

Fig. 7b shows the measurement of the Au(111) Fermi surface contour using a pass energy of 30 eV and integrating the data over a duration of 10 minutes. Both images show a very similar resolution, where the Au states appear sharper in the image measured using the double pass mode. This is due to the better energy resolution of the analyzer which is nominally $\Delta E = 10$ meV using Eq. 38 with an effective radius of the double pass analyzer of $R_0^{double} = 300$ mm. To obtain the same energy resolution in the aberration compensated configuration would require a pass energy of 15 eV. Despite the much better energy resolution compared to Fig. 7a, the measurement took only about half of the acquisition time.

For the aberration compensated configuration an ultimate energy resolution of 12 meV has been measured for 15 eV pass energy (see Fig. 8a) [3]. In the case of the double pass configuration, we find here a comparable ultimate resolution of 13 meV at 30 eV pass energy, as displayed in Fig. 8b by the energy profile of the Fermi edge of the Au (111) sample. Taking into account the finite width of the Fermi edge at the sample temperature of 20 K, these values are in good agreement with the expected resolution.

The new double pass configuration of the imaging HDA allows to use a twice larger pass energy in order to obtain the same energy resolution as with the conventional double HDA. Since the transmission of the analyzer for a given slit size scales with the square of the pass energy, $Tr \sim (E_{Pass})^2$, the double pass configuration results in a 4 times increased measurement speed. This substantially increased measurement efficiency enables new high resolution experiments, particularly when using laboratory based light sources, such as upcoming laser based light sources for photoemission employing high harmonic generation, but also for conventional gas discharge light sources.

As an example, we have measured the spectral function $I(k_x, k_y, E)$ of the Au(111) crystal surface in a wide energy range from the Fermi energy to 7 eV below E_F. Fig. 9 shows a section thorough the three-dimensional spectral function along the $\bar{M} - \bar{\Gamma} - \bar{K}$ directions of the surface Brillouin zone. The total experimental data set consists of 300 constant energy (k_x, k_y) momentum disks acquired each for 60 s. This results in a total measurement time of only 5 h using excitation by He-I radiation from the gas discharge lamp. It needs to be noted that the energy resolution of the double pass HDA was set to the best demonstrated value of $\Delta E = 13$ meV, as it was also used in Fig. 7b. Therefore, even in this wide energy range overview measurement, small details of the Au(111) band structure are revealed. For instance, one can observe the Rashba splitting of the well known Shockley surface state [24], or straight narrow lines of reduced intensity in the range of E_F-3 eV to E_F-7 eV related to the electron interference in surface barrier scattering [25,26].

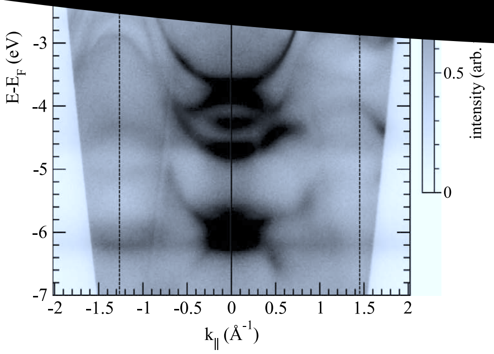

Fig. 9. Measured spectral function along the $\bar{M} - \bar{\Gamma} - \bar{K}$ direction of the Au (111) surface. The measurement consists of a total of 300 energy slices measured at a resolution of $\Delta E = 13$ meV. The total measurement time was 5 h.

6. Conclusions

In summary, we have presented analytical expressions to describe the imaging properties of hemispherical deflection analyzers for use in high resolution imaging electron microscopy and momentum microscopy. From the calculations, the energy resolution and nonisochromaticity of the imaging energy filter can be directly evaluated and was found to be in excellent agreement with experimental results. The nonisochromaticity is a general image aberration of imaging energy filters. It leads to a nonuniform energy distribution over the field of view, such that an image is not strictly monochromatic. In the case of the HDA, the nonisochromaticity comes about by the α^2 sphere aberration in the dispersive plane of the analyzer, and therefore is equally present for a single HDA, an aberration compensated HDA, as well as for the double pass HDA. However, this nonisochromaticity is a simple expression depending only on the square of one in-plane image coordinate, and can be easily corrected numerically. In particular, the analytical expressions show that higher order aberration terms are absent for both in-plane image coordinates. This represents an important advantage of the HDA imaging energy filter for high resolution electron microscopy applications.

The solutions for the electron trajectories in the analyzer further show that aberrations that were previously believed to limit the image resolution [7] cancel out when taking into account the refraction of electrons at the entrance- and exit-slits of the analyzer. The fringe field at the entrance and exit of the analyzer is known to introduce a focusing effect of the electron trajectories that shifts the focal point to deflection angles $< 180°$, leading to a crossover in front of the slit plane inside the analyzer [16]. Previous studies have concentrated mainly on reducing this fringe field effect on the position coordinate ρ_π, in order to increase the performance of the analyzer, e.g., by using biased analyzers [22] or paracentric entry geometries [22,23]. In contrast, our results show that refraction of the electron trajectories due to the fringe field changes the trajectory angles exactly in such a way that the sphere aberration gets canceled out for the trajectory angle α. Our experimental results confirm that no discernible image aberrations are introduced for trajectory angles of up to $\pm 3°$. In general, the analytical expressions do not impose a limit on the trajectory angles. Nevertheless for lager angles, attention should be given to the actual form of the fringe fields, in order to avoid effects by higher order aberrations that were not captured analytically.

This previously overlooked effect allows to use a single HDA as an [redacted] proposed double pass configuration. The [redacted] times increased transmission at comparable energy and image [redacted] tion than the aberration compensated analyzer. The double pass configuration is therefore of particular advantage for momentum microscopy with ultimate energy and wave vector resolution.

Coulomb interactions between electrons, that are not captured in the analytically derived expressions, are usually not a limiting factor of the energy analyzer in PEEM or momentum microscopy. The effect of these space charge interactions has been found previously to be dominated by Coulomb interactions in the regions directly above the sample surface [27], as well as inside the objective lens of the microscope [28]. Space charge effects are observed at about 10–100 electrons per pulse, and peak current densities of some $10\frac{\text{nA}}{\mu\text{m}^2}$. These current densities, however, can easily occur in other applications, for instance, when the HDA shall be used as monochromator for intense pulsed electron beams, such that Coulomb effects then need to be considered. This is as well the case for applying the HDA energy filter to ion beams, where the critical current density for space charge broadening gets reduced due to the larger mass of ions compared to electrons [29].

The use of pulsed excitation sources represents an attractive way to increase the detection efficiency, i.e., the ratio between excited electrons and detected electrons. This is nowadays achieved by the use of a time-of-flight (ToF) energy detection scheme, for instance in a ToF momentum microscope [4]. Future combinations of a dispersive band-pass energy selection by a HDA with the simultaneous ToF detection of multiple kinetic energies will open a way to combine the mutual advantages of versatility and efficiency in one instrument. In particular, the perfect refocusing in space and time of the electron trajectories in the aberration compensated HDA [11] provides a non-straight low-energy drift section in which the ToF only depends on the electron energy.

In general, hemispherical deflection analyzers have become an important component for high-resolution momentum microscopy, as well as spectroscopic surface electron microscopy. The detailed understanding of their imaging properties will contribute to further improve the resolution and performance of these experimental techniques and to address current topics in condensed matter science.

Acknowledgements

The authors like to thank Oliver Schaff and Thorsten Kampen (SPECS Surface Nano Analysis GmbH) for their support and discussions

References

[1] E. Bauer, J. Electron Spectrosc. Rel.Phenomena 114–116 (2001) 975–987.
[2] S. Suga, C. Tusche, J. Electron Spectrosc. Relat. Phenom. 200 (2015) 119–142.
[3] C. Tusche, A. Krasyuk, J. Kirschner, Ultramicroscopy 159 (2015) 520–529.
[4] C. Tusche, P. Goslawski, D. Kutnyakhov, M. Ellguth, K. Medjanik, H.J. Elmers, S. Chernov, R. Wallauer, D. Engel, A. Jankowiak, G. Schönhense, Appl. Phys. Lett. 108 (2016) 261602.
[5] F. Hadjarab, J.L. Erskine, J. Electron Spectrosc. Relat. Phenom. 36 (1985) 227–243.
[6] A. Locatelli, E. Bauer, J. Phys. 20 (2008) 093002.
[7] B.P. Tonner, Nucl. Instrum. Methods Phys. Res., Sect. A 291 (1990) 60–66.
[8] M. Escher, N. Weber, M. Merkel, C. Ziethen, P. Bernhard, G. Schönhense, S. Schmidt, F. Forster, F. Reinert, B. Krömker, D. Funnemann, J. Phys. 17 (2005) S1329–S1338.
[9] D. Funnemann, M. Escher, Energy filter image generator for electrically charged particles and the use thereof, European patent EP1559126B1 (2007).
[10] B. Krömker, M. Escher, D. Funnemann, D. Hartung, H. Engelhard, J. Kirschner, Rev. Scient. Instrum. 79 (2008) 053702.
[11] M.J. Pellin, C.E. Young, D.M. Gruen, Scanning Microsc. 2 (1988) 1353–1364.
[12] C. Tusche, J. Kirschner, Abbildende Energiefiltervorrichtung und Verfahren zu deren Betrieb, German patent, DE102014019408B4 (2016).
[13] A. Baraldi, V. Dhanak, J. Electron Spectrosc. Relat. Phenom. 67 (1994) 211–220.
[14] T. Fließbach, Mechanik: Lehrbuch zur Theoretischen Physik I, 5th edition, Spektrum Akademischer Verlag, 1999. Chapter 17
[15] H. Goldstein, C.P. Poole, J.L. Safko, Classical Mechanics, 3rd edition, Addison Wesley, 2000. Chapter 3
[16] D. Roy, D. Tremblay, Rep. Prog. Phys. 53 (1990) 1621–1674.
[17] P. Louette, A. Delage, D. Roy, P. Thiry, R. Caudano, J. Electron Spectrosc. Relat. Phenom. 52 (1990) 867–874.
[18] H. Wollnik, H. Ewald, Nucl. Instrum. Methods 36 (1965) 93–104.
[19] C. Wiemann, M. Patt, I.P. Krug, N.B. Weber, M. Escher, M. Merkel, C.M. Schneider, e-J. Surf. Sci. Nanotechnol. 9 (2011) 395–399.
[20] C.T. Koch, W. Sigle, R. Höschen, M. Rühle, E. Essers, G. Benner, M. Matijevic, Microsc. Microanal. 12 (2006) 506–514.
[21] E. Essers, G. Benner, T. Mandler, S. Meyer, D. Mittmann, M. Schnell, R. Höschen, Ultramicroscopy 110 (2010) 971–980.
[22] O. Sise, M. Ulu, M. Dogan, G. Martinez, T.J. Zouros, J. Electron Spectrosc. Relat. Phenom. 177 (2010) 42–51.
[23] O. Sise, T.J.M. Zouros, J. Spectrosc. 2015 (2015) 153513.
[24] J. Henk, A. Ernst, P. Bruno, Phys. Rev. B 68 (2003) 165416.
[25] A. Winkelmann, M. Ellguth, C. Tusche, A.A. Ünal, J. Henk, J. Kirschner, Phys. Rev. B 86 (2012) 085427.
[26] A. Zaporozhchenko-Zymaková, D. Kutnyakhov, K. Medjanik, C. Tusche, O. Fedchenko, S. Chernov, M. Ellguth, S.A. Nepijko, H.J. Elmers, G. Schönhense, Phys. Rev. B 96 (2017) 155108.
[27] G. Schönhense, K. Medjanik, C. Tusche, M. de Loos, B. van der Geer, M. Scholz, F. Hieke, N. Gerken, J. Kirschner, W. Wurth, Ultramicroscopy 159 (2015) 488–496.
[28] A. Locatelli, T.O. Menteş, M.A. Niño, E. Bauer, Ultramicroscopy 111 (2011) 1447–1454.
[29] C. Tusche, J. Kirschner, Rev. Sci. Instrum. 85 (2014) 063305.